

PROCEEDINGS OF SPIE

[SPIDigitalLibrary.org/conference-proceedings-of-spie](https://spiedigitallibrary.org/conference-proceedings-of-spie)

ESA's CCD test bench for the Euclid visible channel

Peter Verhoeve, Nathalie Boudin, Udo Telljohann, Tim Oosterbroek, Didier Martin, et al.

Peter Verhoeve, Nathalie Boudin, Udo Telljohann, Tim Oosterbroek, Didier Martin, Ludovic Duvet, Thierry Beaufort, Bart Butler, Isabel Escudero-Sanz, Hans Smit, Fritz de Wit, "ESA's CCD test bench for the Euclid visible channel," Proc. SPIE 8453, High Energy, Optical, and Infrared Detectors for Astronomy V, 845322 (25 September 2012); doi: 10.1117/12.926016

SPIE.

Event: SPIE Astronomical Telescopes + Instrumentation, 2012, Amsterdam, Netherlands

ESA's CCD test bench for the Euclid visible channel

Peter Verhoeve^{*a}, Nathalie Boudin^{a,b}, Udo Telljohann^a, Tim Oosterbroek^a, Didier Martin^a, Ludovic Duvet^a, Thierry Beaufort^a, Bart Butler^a, Isabel Escudero-Sanz^a, Hans Smit^a, Fritz de Wit^a

^a *Future Missions Preparation Office, ESA/ESTEC, P.O. Box 299, 2200 AG Noordwijk, The Netherlands;*

^b *Cosine Research BV, Niels Bohrweg 11, 2333 CA Leiden, The Netherlands*

ABSTRACT

The visual imaging instrument VIS on board Euclid baselines 36 newly designed CCD273-84 devices from e2v. While these new devices have a 4kx4k format with four readout nodes, the Euclid Imaging Consortium (EIC) has performed extensive test campaigns on both irradiated and un-irradiated devices of the 4kx1k Euclid precursor variant CCD204-22. In support of the CCD development and characterization, and to enable an independent assessment of the Euclid CCDs (the procurement of which is ESA's responsibility), ESA/ESTEC has built a test bench. This test bench allows for a flexible operation and readout of the CCDs, originally for CCD204 and shortly also for CCD273-84. It provides the basic tools for noise and gain calibration, and CTI, QE, MTF and PRNU measurements. In addition, the bench provides scanning spot illumination with a spot size well below the pixel size, for measurement of the intra-pixel response of the CCDs before and after radiation damage. Such measurements are of great importance for the characterization and modeling of the VIS instrument's PSF, in particular to enable the prediction of the evolution of the PSF shape under the influence of the L2 radiation environment during the mission. This set-up will also allow for simulation of typical Euclid sky images in the lab. The capabilities and validation of this bench at ESA are described in this paper.

Keywords: Euclid, CCD, astronomy

1. INTRODUCTION

Euclid is an ESA mission designed to measure the expansion history of the Universe and the growth of cosmological structures, and understand the origin of Universe's accelerating expansion. For this purpose it uses two cosmological probes, Weak Lensing and galaxy clustering. The mission will observe galaxies and clusters of galaxies out to a red-shift of $z \sim 2$, in an all-sky survey covering 15 000 deg². It consists of a 1.2m diameter Korsch telescope with two focal plane instruments: a visual imager (VIS) and a near-IR spectro-photometer (NISP). Both instruments share a common field of view of 0.54 degrees². Euclid will be launched in 2020, for 6 years of operation at the Sun-Earth L2 point. A further description of the Euclid mission, currently at the beginning of phase B2, and its status is given in Laureijs et al. [1].

The VIS instrument consists of a CCD-based focal plane array, with a shutter mechanism to close the optical path during read out and dark calibration, and a calibration unit for flat field measurements. It covers the wavelength range of ~550-920 nm as a single wide band. The FPA supports 6x6 CCDs (4kx4k pixels each) with a plate scale of 0.101 arcsec/pixel giving a geometric field of 0.55 deg² (including the gaps between the CCDs). With the Weak lensing technique, the VIS channel measures the shapes of galaxies with about 0.16 arcsec (FWHM) system point-spread function excluding pixelisation. This technique requires an unprecedented accuracy to which the shapes of the galaxies have to be measured. In particular, radiation damage effects in the CCDs will challenge this accuracy during the mission. A detailed description of the VIS instrument can be found in Cropper et al [2].

The NISP instrument's FPA consists of an array of 4x4 HgCdTe NIR detectors (2kx2k pixels each) with 0.3 arcsec per pixel covering an area of ~0.55 deg². It can be operated in either photometer mode or slitless spectrometer mode by means of filterwheels. In photometer mode NISP images the sky in three filterbands (Y, J, H) covering the wavelength range 0.92-2.0 micron. In the slitless spectrometer mode, the light is dispersed by means of grisms in the wavelength range 1.1 to 2.0 micron at a constant spectral resolution $\lambda/\Delta\lambda \sim 250$. Two kinds of grisms with different passbands are used: two blue grisms transmit between 1.1 and 1.45 micron, while the two red grisms are transparent between 1.45 to

* peter.verhoeve@esa.int;

2.0 micron. Both sets of gratings are mounted in 0 and 90 deg orientation. A description of the spectrometer part of the NISP is provided by Prieto et al [3].

ESA will be responsible for the procurement of the detectors for VIS (CCD273 from e2v) and, in collaboration with NASA, for the detectors of NISP (HAWAII 2RG, from Teledyne). ESA/ESTEC has built in-house test benches for CCDs and the HAWAII 2RG detectors, which are foreseen to support detector development and characterization, and to enable an independent assessment of the Euclid detectors. The test bench for the NISP detectors is described in [4]. This paper is dedicated to the test bench for the VIS CCDs. While the bench is currently dedicated to Euclid CCD testing, it is flexible enough to accommodate other CCD types, as may be required for future missions or technology development activities. Test results on prototype Euclid CCDs obtained with this test bench are given in an accompanying paper in these proceedings [5].

2. DESCRIPTION OF THE CCD TEST BENCH

The CCD test bench consists of a CCD cryostat, a CCD controller, a versatile illumination system and a PC-based control system. The cryostat and the illumination system are placed in a dark enclosure mounted on an optical table with vibration control through pneumatic isolators.



Figure 1: The CCD cryostat with vacuum enclosure removed (upside down). The plate with the regular grid of threaded holes is the bottom of the liquid nitrogen reservoir and acts as the sample stage for the CCD. The cylindrical enclosure is a 77K thermal shield, with an aperture for radiation access on the left hand side. The inset shows a Euclid prototype FI CCD273-84 as seen through the radiation access port of the cryostat.

2.1 Cryostat

The CCD cryostat is a liquid nitrogen cooled system, originally built for liquid helium operation. It has a 12 liter liquid nitrogen reservoir, the bottom of which is used as sample stage (in vacuum) with a diameter of ~24 cm, see Figure 1. The CCD and its Front End Electronics (FEE) are mounted on an Al bracket which has a thermal impedance to the 77K base plate. The sample stage is completely enclosed by 77K shields, with an opening in front of the CCD for radiation access. The CCD's temperature is monitored and PID controlled with a resistive heater on the Al bracket. The FEE board is thermally disconnected from the Al bracket and held within its nominal operating temperature range with a separate heater. The Al bracket can be replaced by a similar bracket out of Ti, which provides a better CTE match to the SiC

package of the Euclid CCDs. Not included in the pictures in Figure 1 are black shields around the CCD, which act as stray light baffles for light entering the cryostat, that is not absorbed by the CCD. The time required to cool down the CCD from ambient temperature to $\sim 150\text{K}$ and stabilize to within 0.1 K from the target temperature is about 4 hours, while changing the temperature by 10K and stabilizing again takes about 2 hours. The ultimate temperature stability is better than 10 mK over many hours.

2.2 CCD controller

The CCD controller and FEE are procured from XCAM Ltd (UK). It provides bias voltages and clocks from separate bias and clock driver cards. Clocks and Correlated Double Sampling (CDS) timing sequences with a time resolution of about 30 ns are generated from an ADSP 2181 chip on the clock driver card. The video signals from the CCD are pre-amplified ($5\times$) on the FEE electronics board in the cryostat, and then fed into a Dual Slope Integrator CDS/ADC card with a 16-bits ADC chip. Currently, a single channel is available, but a 4-channel version designed for readout of the Euclid CCD273-84 is in fabrication. The noise limit of the system (excluding the CCD noise contribution) amounts to $\sim 3\text{ DN rms}$.

2.3 Control Software

The CCD test bench is controlled via a dedicated Python 2.7 script. The script's main function is to provide: temperature control, system monitoring, test bench configuration, data acquisition and sequence control. The software uses "PyGTK" as its GUI interface, "SciPy" for data analysis, and "Matplotlib" for data visualization. The serial communication to the various instruments included in the test bench uses "PyVisa" to interface with GPIB + RS232 devices. The XCAM CCD controller is controlled by a "QuickUSB" driver that has been integrated into a high-level Python API to handle data acquisition and configuration. The software was designed to be modular and easily extended. This was accomplished by breaking down the code into 4 distinct layers: low level hardware communication, high level I/O API, sequence logic, and a GUI which acts as a "dumb" terminal to display: log files, strip charts, images, configuration and data acquisition control. The GUI is dynamically generated using configuration files, which provides a high degree of control and flexibility. Each I/O device is wrapped in a high level interface that provides additional functionality such as: I/O simulation, remote TCP/IP control, and communication logging.

A few modifications were made to the XCAM controller sequencer code (ADSP code) to optimize the synchronization with the PC. A set of signals, available from the controller and controlled within the sequencer, is used to implement a simple form of handshaking between the PC and the XCAM rack. These signals are used to communicate the DSP state through the controller's 15 pin I/O port to the PC's printer port. The CCD image exposure timing is now managed through the ADSP 2181 timer interrupt. The timer interrupt is used to signal when CCD integration starts and stops. It extends the range of integration time, and also provides a more accurate timing mechanism. This implementation also allows the integration cycle to be cancelled.

Other devices and processes under control of the Python application are: CCD temperature controller, temperature readout, monochromator wavelength setting and filter selection, shutters, translation stages and power readout from reference photodiodes.

Acquired CCD images are stored in FITS format files, the header section of which contains information on the operating conditions of the CCD (bias voltages, sequencer file), illumination (source, wavelength), temperatures and pressure, etc. Some basic quick-look tools provide image display with cross-section analysis, histogramming and Gaussian fitting for noise analysis. Apart from the CCD images, also log files of housekeeping data (temperatures etc), command history and exposure lists are continuously logged.

The control software allows for a high degree of automated measurement series through nested loops of parameter variations. Examples of such fully automated series are: dark signal or x-ray illumination as a function of CCD exposure time for a range of temperatures (including temperature stabilization), noise and gain measurements as a function of two or three bias voltages, or quantum efficiency measurements as a function of wavelength, including reference detector measurements.

2.4 Dark measurements and x-ray illumination mode

For dark and x-ray measurements, the entrance port of the cryostat is closed with a metal blind flange. In this condition, and with pressure gauges switched off, the residual light intensity as measured on the CCD, is well below 10^{-5} photons/s/pixel (for $12 \times 12 \mu\text{m}^2$ pixels). An x-ray source (either ^{55}Fe with photon energies $E=5.9$ and 6.4 keV, or ^{109}Cd with $E \sim 22$ keV) with a programmable shutter is mounted in the middle of the flange. The (mostly used) ^{55}Fe source provides a maximum intensity of about 10^{-2} x-ray photons/s/pixel. The well-known energies of the x-ray photons allow for independent, calibrated measurements of the system gain and noise, which in turn are needed to optimize the CCD bias voltages for lowest noise operation. In addition, x-ray images provide a useful diagnostic for verifying correct CCD operation (in particular charge transfer) and for measuring the charge transfer in-efficiency (CTI) under various operating conditions and modes. An example of such analysis from x-ray spectra acquired with a front-illuminated prototype Euclid CCD273-84 is shown in Figure 2.

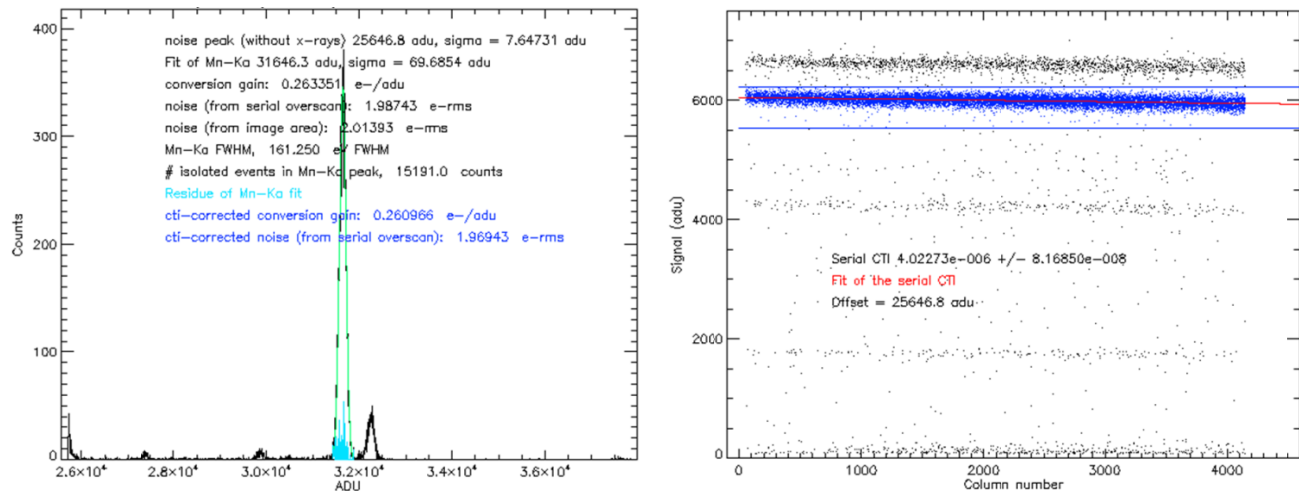


Figure 2: left: example of an x-ray spectrum (^{55}Fe , single pixel events selected). Right: CTI analysis for the serial register with the same x-ray data

2.5 The uniform illumination system

To evaluate the basic optical performance parameters (quantum efficiency (QE), response linearity, response uniformity, noise, conversion gain, full well capacity, CTE) we use a setup that provides a uniform illumination of the CCD with tunable narrowband light. Figure 3 shows a schematic of the test bench in its uniform illumination mode. The light source is a 100W Quartz-Tungsten-Halogen (QTH) lamp. Wavelength selection in the range $\lambda=200-1050\text{nm}$ is done with a grating monochromator (ORIEL Cornerstone 130), complemented with higher order suppressing filters. The bandwidth can be tuned (manually) with slits from 2-20 nm (FWHM). The output of the monochromator is coupled into a fibre bundle, which delivers the light into an Integrating Sphere (ORIEL 70667, useful wavelength range 350-1300nm) with a 50 mm diameter output port. The CCD in the cryostat is at ~ 83 cm from the exit port of the integrating sphere. There are two reference detectors (Si photodiodes): one (RD2 in Figure 3) is at a fixed off-axis position for continuous relative intensity monitoring, the other one (RD1 in Figure 3) is on a 3-axis translation stage about 10 cm in front of the CCD. The latter one has a calibrated responsivity and a well-defined entrance aperture and is used as reference detector in QE measurements. The height and lateral position of the CCD are fixed, but the cryostat has some tip/tilt adjustment. The integrating sphere and the calibrated reference detector have full translational and rotational alignment facilities, so as to ensure that all detector planes can be aligned orthogonally to the optical axis of the integrating sphere.

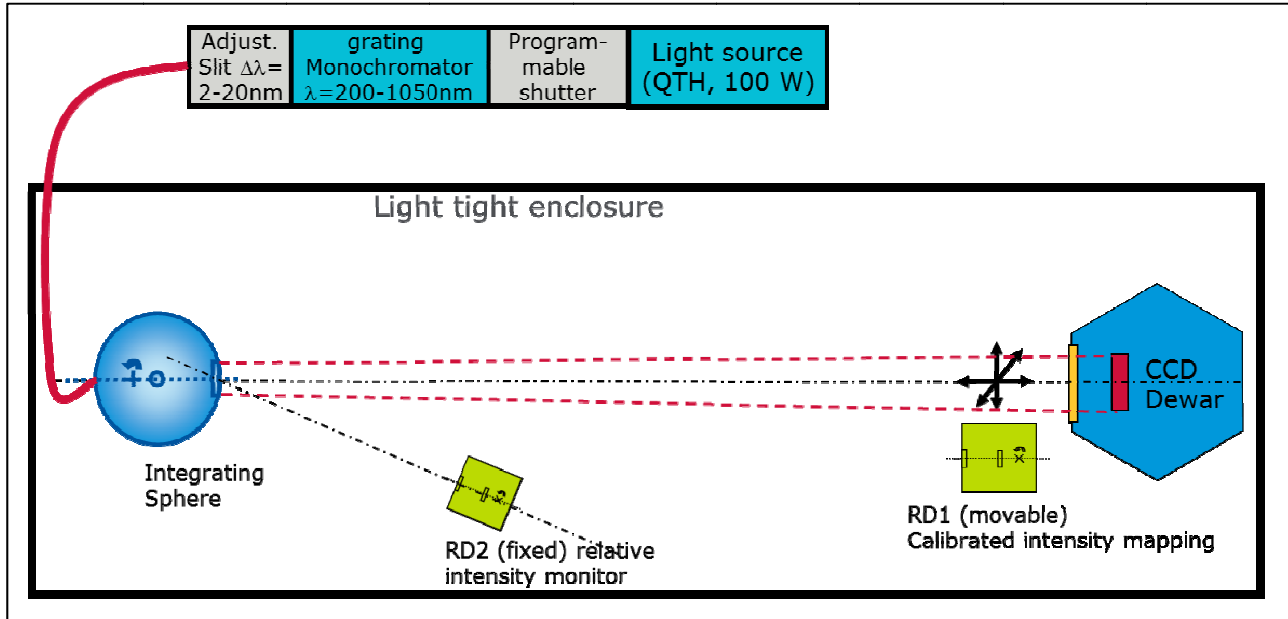


Figure 3: schematic of the uniform illumination setup (see text for further details).

The reference detector RD1 has been used to map the intensity distribution in planes orthogonal to the optical axis, and over a wide range of positions along the optical axis. The result of this calibration is shown in Figure 4. The intensity maps in this figure have been corrected for any background and for drift in the source intensity (using the fixed monitor RD2). They show that the intensity distribution over a Euclid sized CCD ($50 \times 50 \text{ mm}^2$) is uniform to well within 1%, and that the intensity scales with $(1/\text{distance})^2$ very accurately. This enables us to calculate the absolute intensity at the (known) position of the CCD from the measured intensity at the (known) position of the calibrated reference photodiode (RD1) with an estimated accuracy of a few percent. Further corrections to this calculated intensity come from the finite transmission of the cryostat window and the refraction of the non-collimated beam through the window. The cryostat window is a 10 mm thick AR-coated slab of fused silica with a clear aperture diameter of 80 mm. The measured transmission of the window is $>96\%$ over the wavelength range $\lambda=400\text{-}1100\text{nm}$ (see Figure 6). The typical intensity of the source in the range $\lambda=400\text{-}1050\text{nm}$ (with $\Delta\lambda=10\text{nm}$) at the position of the CCD corresponds to $\sim 1000\text{-}7000$ photons/s/pixel incident on the CCD, and scales linearly with the bandwidth $\Delta\lambda$.

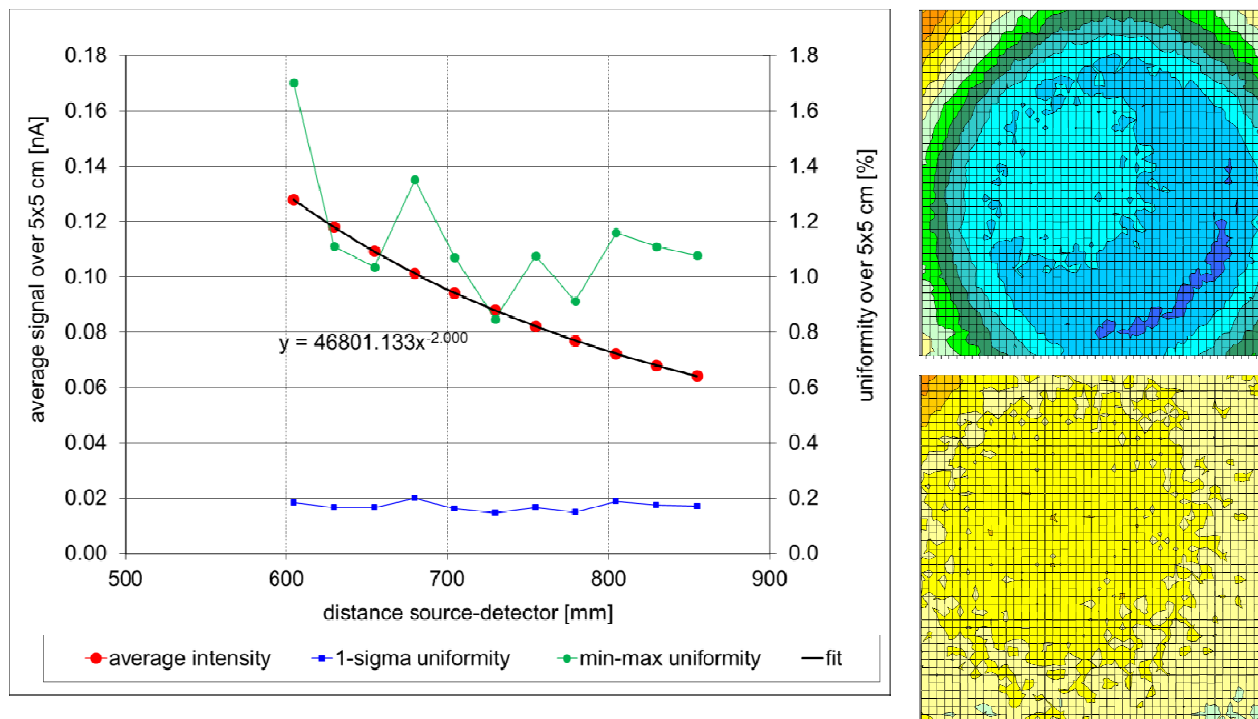


Figure 4: right: Measured intensity distribution in $90 \times 90 \text{ mm}^2$ planes orthogonal to the optical axis at 610 mm (top) and 830 mm (bottom) from the exit port of the integrating sphere. Adjacent contours represent 0.5% variation in intensity. Left: Intensity and uniformity (over a $50 \times 50 \text{ mm}^2$ area) as a function of distance from the source.

A series of CCD images acquired under uniform illumination over a large range of intensities (usually realized by varying the exposure time) can be used to construct a photon transfer curve (PTC), which represents the relationship between average pixel value (= signal) and variance of the pixel values, both expressed in Digital Numbers (DN). Since the three main contributors to the variance (read noise, photon statistics and pixel response non-uniformity (PRNU)) have a different dependence on the signal (independent, linear and quadratic, respectively), these can be deduced unambiguously from the PTC. Figure 5 shows two PTCs, derived from the same series of images acquired with a FI prototype Euclid CCD273. One curve is the results from a 3500×1100 pixels large area, while the other results from a 500×500 pixel area. A fit to the data yields the same contribution from photon statistics and read-out noise (~ 3.6 DN rms), but a slightly different value for the PRNU: 0.96% rms and 0.79% rms, respectively. Repeating the analysis for smaller areas does not yield lower values for PRNU, suggesting that real CCD PRNU is $\sim 0.8\%$. The larger value found for the larger area may then be attributed to $\sim 0.5\%$ rms non-uniformity of the illumination over that area.

As another example of an experiment performed with the uniform illumination setup, Figure 6 shows the results of a QE measurement on a Euclid prototype, front-illuminated (FI) CCD273-84 (without AR coating). The CCD temperature was 153 K. The estimated relative accuracy of the measurements is $\sim 5\%$. This estimate is based on an error budget which includes the uncertainties of detector positions, photodiode calibration, window transmission, intensity map interpolation and CCD gain calibration. There is a reasonable agreement with the e2v provided curve for a standard, deep-depleted FI device at ambient temperature. Due to the increase in band gap energy at lower temperature, the efficiency beyond 800 nm is indeed expected to decrease at lower temperatures. Nevertheless, QE measurements on back-illuminated devices indicate a systematic overestimate of the QE by 5-10%. We are currently investigating this issue.

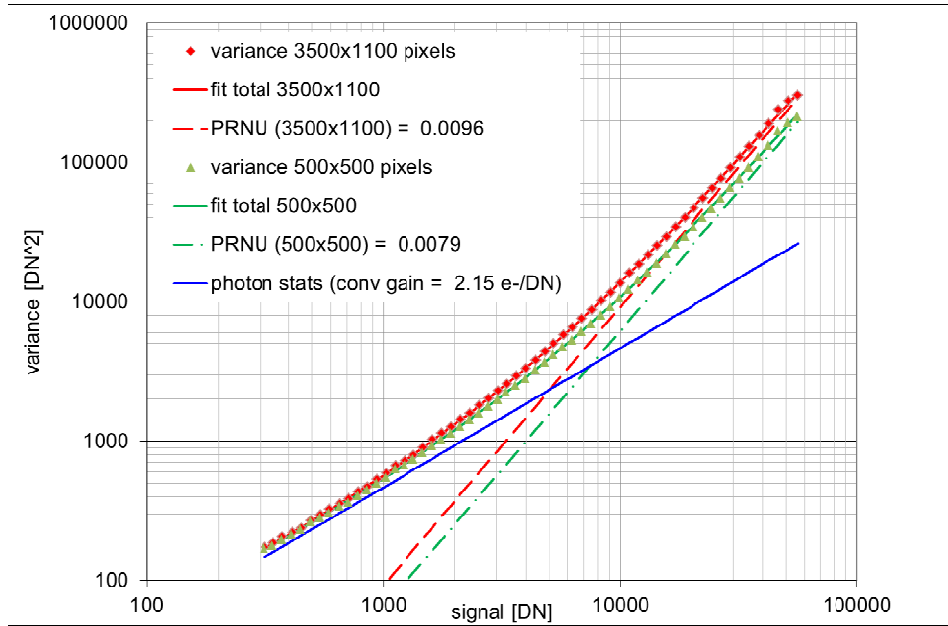


Figure 5: Photon Transfer curves derived from the same series of images, but from the analysis of a large area (3500x1100 pixels, in red diamonds) and of a small area (500x500 pixels, green triangles). The difference in PRNU between the two sets is due to residual non-uniformity in the illumination. The data were acquired with a FI prototype Euclid CCD273.

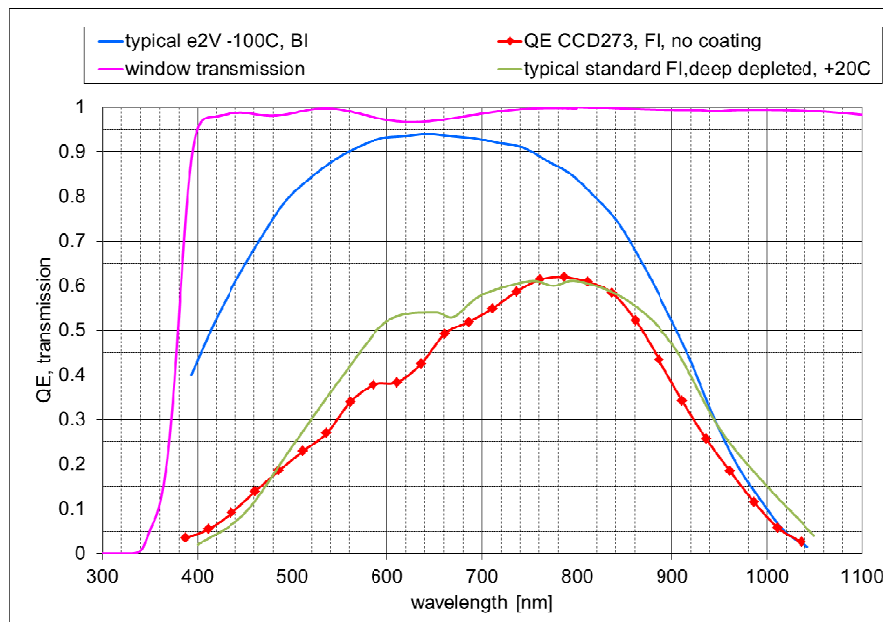


Figure 6: The measured QE of a Euclid prototype front illuminated CCD273-84 at T=153K (no coating) red diamond symbols. The green curve represents the QE of a typical standard deep depletion front illuminated CCD at T=+20C, the blue line represent a back-illuminated CCD at T=173K. The transmission of the fused silica cryostat window is indicated with the purple line.

2.6 The spot illumination system

In the spot illumination configuration, the Integrating Sphere as a light source is simply replaced by a pinhole mask illuminated with an LED. The pinhole mask is imaged onto the CCD with a triplet lens (Newport PAC076). The same translation stages that carry the photodiode RD1 (Figure 3) are used to align and focus the projected image. The pinhole mask consists of a stainless steel metal sheet with laser-drilled holes with a nominal diameter of $20\ \mu\text{m}$ at a regular grid with a pitch of $0.85\ \text{mm}$. The diameter of the mask is $\sim 25\ \text{mm}$. When projected on the CCD, the spots have a size of ~ 2.5 pixels FWHM, similar to what is expected for the images of small galaxies in the Euclid VIS instrument. This allows us to investigate how the shape of an imaged galaxy may change due to degradation of the charge transfer efficiency (CTE) induced by radiation damage over the duration of the Euclid mission. To test this, we used a back-illuminated CCD204-22 (4096×1024 pixels) which was partially irradiated with two different doses of $10\ \text{MeV}$ equivalent protons (see Figure 7, lower panel). Note that the irradiation included the serial register, which is in the horizontal direction of Figure 7. The pinhole mask was projected onto the left side of the CCD, partially overlapping the irradiated area #1 and the two un-irradiated areas on either side of this. The CCD has two outputs, one on either side of the serial register. Two sets of 100 images were taken, one with readout to the left, the other with readout to the right, without changing the illumination conditions in between. The pixel rate was $185\ \text{kHz}$ and the CCD temperature was $155\ \text{K}$. The images of each set were co-added to improve the photon statistics, without loss of spatial resolution. The top panel of Figure 7 shows the co-added image from the set with readout through the left side output stage.

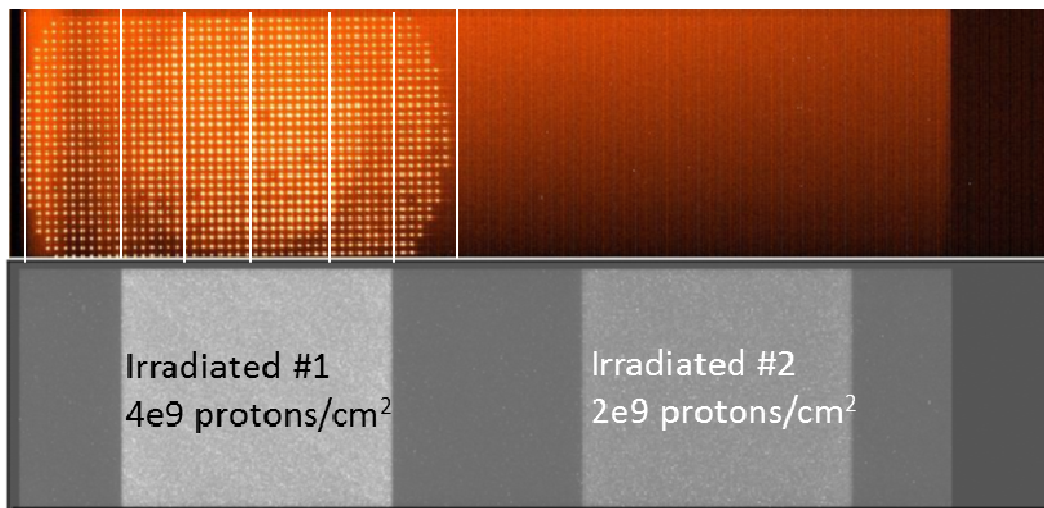


Figure 7: bottom: Dark signal image of the irradiated CCD204-22 (taken at $205\ \text{K}$, $3000\ \text{s}$ exposure time) showing the elevated dark signal levels in the two irradiated areas. The darker regions on the left, top and right are pre-scan and overscan pixels. Top: resulting image from 100 co-added images illuminated with the pinhole mask. Intensity variations are due to non-uniformity in the illumination of the mask, and of the mask itself. The vertical white lines define the 6 regions used for the analysis. Both images were acquired with readout towards the left hand side.

A zoom-in of part of the image (see Figure 8), clearly shows the increasing intensity of the charge trails in the horizontal direction, corresponding to an increasing number of transfers through the irradiated zone #1 of the serial register. The illuminated region is divided in six subsections, as indicated with the white lines in the top panel of Figure 7. This choice of subsections along the horizontal direction implies that all information on PSF variation in the vertical direction is lost in this analysis. For each region all spots are centroided separately, aligned and co-added, resulting in 6 average PSFs, as shown in the lower panel of Figure 8. Clearly, the leftmost PSF, representing spots that have not been transferred through irradiated areas, show no charge tails. The next four PSFs show increasing horizontal charge tails, as expected from the larger number of transfers through the irradiated area, and (fainter) vertical charge tails. The rightmost PSF shows horizontal charge tails only. Note that the charge tails on the left hand side of the PSFs originate from adjacent spots on the left, and are much weaker than the tails on the right.

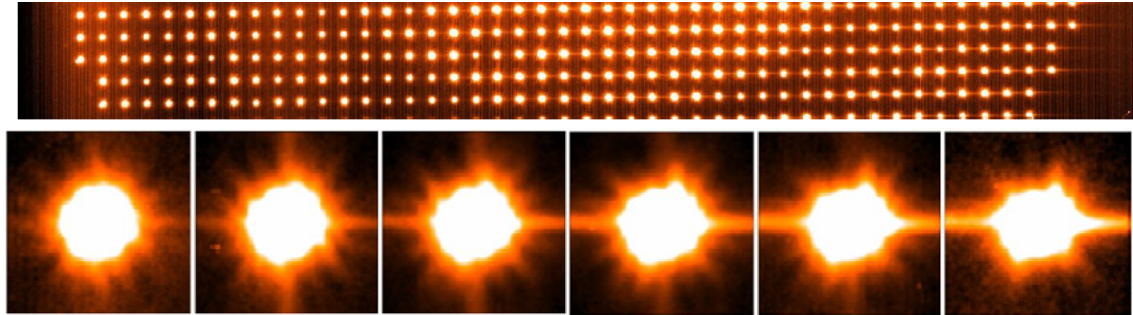


Figure 8: Top: zoom-in on the co-added image from Figure 7, showing the increasing horizontal charge trails towards the right. Bottom: averaged PSFs for each of the six regions defined in Figure 7. The symmetric pattern of streaks is related to the 16-blade adjustable aperture in the setup.

A similar set of six averaged PSFs (corresponding to physically the same regions on the CCD) is derived from the set of images obtained with readout towards the right hand side output stage.

The PSF shapes are then analyzed in terms of ellipticity parameters ϵ_1 and ϵ_2 (with subscripts 1 and 2 referring to $0^\circ/90^\circ$, and $45^\circ/135^\circ$ directions, respectively) and R^2 , following the same recipe as defined for Euclid (see [6], and using a weighting function with a sigma of 0.75). In the ideal case of a perfectly uniform pinhole mask and perfect imaging, the variation in shape over the 6 regions could be directly related to the average number of transfers through the irradiated area. Currently, the variations in PSF appear to be dominated by optical imperfections, rather than by radiation damage induced effects. However, since we have data sets for readout in two opposite directions, we can eliminate the ‘optical’ variations by evaluating the differences for each parameter from the two data sets (corresponding to the readout in the two directions). We are then left with variations due to the different number of transfers through the two irradiated areas. These differences in ellipticity and R^2 are plotted in Figure 9.

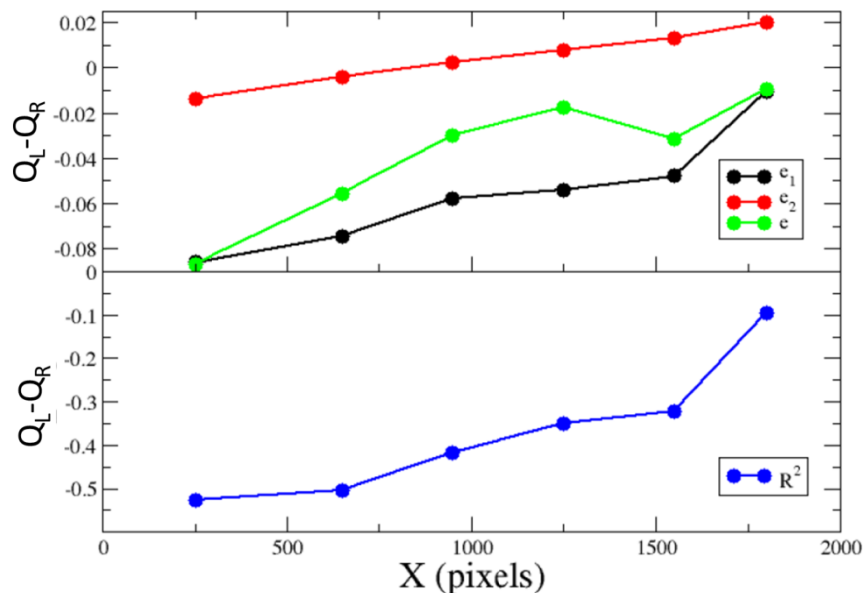


Figure 9: The difference in ellipticity (top) and R^2 (bottom) for the 6 regions defined in Figure 7, derived from the results obtained with readout to the left and right hand side output nodes.

From the data in Figure 9 and the corresponding number of transfers through the two irradiated areas we evaluate the sensitivity of the parameters for radiation damage. The results are shown in Table 1. With the exception of ϵ_2 , the sensitivity for change to transfer through an irradiated area appears to scale with the radiation dose. Since ϵ_2 is related to

the vertical direction, no change would be expected upon transfer in the horizontal direction. However, some change may be induced by the change in centroid that occurs when ϵ_1 changes, or, alternatively, as a residual from the removal of the large ‘optical’ contribution. Extrapolating the results to the maximum number of transfers (~ 2100) through an irradiated area with a dose of 4×10^9 protons/cm², we find $\sim 5\%$ change in ϵ_1 , and an increase of R^2 by 0.3 pixel^2 . The latter should be compared to a total instrument budget for VIS on Euclid of 0.2 pixel^2 .

Table 1: Sensitivities of the ellipticity and R^2 parameters for transfer through the two irradiated areas.

parameter	Sensitivity to transfer		
	$2 \times 10^9 \text{ protons/cm}^2$	$4 \times 10^9 \text{ protons/cm}^2$	
ϵ_1	0.9×10^{-3}	2.5×10^{-3}	% / transfer
ϵ_2	-1.7×10^{-3}	1.2×10^{-3}	% / transfer
ϵ	0.8×10^{-3}	2.5×10^{-3}	% / transfer
R^2	0.8×10^{-4}	1.5×10^{-4}	Pixel ² / transfer

The accuracy of the method is currently limited by the relatively large ‘optical’ variations, and the clock patterns have not been optimized for mitigation of CTI degradation. Therefore the results should be regarded as very preliminary. Also, further improvements of the method are foreseen with the use of more uniform pinhole masks and better optical alignment and imaging quality.

2.7 The subpixel spot illumination system

For Euclid VIS to be able to measure the shapes of galaxies to the required accuracy, it is of extreme importance that the instrument Point Spread Function (PSF) is known with great precision as well. For this purpose we have designed and built a spot projector that can provide spot sizes well within the pixel size of $12 \mu\text{m}$ of the Euclid CCDs over the Euclid VIS wavelength range of interest $\lambda=550\text{-}920 \text{ nm}$. Figure 10 shows how this spot projector will be integrated in the CCD test bench. The spot projector setup consists of:

- a pinhole, illuminated with a monochromatic (or narrow-band) source through an optical fibre, The size of the pinhole is $5 \mu\text{m}$ or smaller to ensure that the performance of the optics is not compromised
- a field stop, the size of which can be adapted to mimic the Euclid optical configuration
- a 6-component optic mounted in a single mechanical assembly, built by Jenoptik Optical Systems (Germany). The optical design is shown in the insert of Figure 10. The optic has a magnification of ~ 0.5
- A mount on which the above three components are mounted. It includes tip/tilt facilities for alignment of the entire unit, as well as separate micrometer driven alignment stages for the pinhole
- A 3-axis translation stage using Newport MTM100 precision motors with a range of 100mm , a resolution of $0.1 \mu\text{m}$ and a position accuracy of $\sim 1.5 \mu\text{m}$. This stage is used to focus the spot on the CCD and perform scans across the CCD with micrometer resolution
- The entire setup is mounted on a vibration controlled optical table in a dark enclosure. The ambient temperature inside the enclosure can be controlled to ensure good thermo-mechanical stability of the set-up.
- In this configuration the CCD cryostat is equipped with an 8 mm thick sapphire vacuum window. The window is recessed into the cryostat vacuum so as to reduce the distance between the spot projector and the CCD. It has a clear aperture diameter of $\sim 60\text{mm}$ and an AR coating with a minimum transmission of 94.6% over the range $\lambda=550\text{-}920 \text{ nm}$.

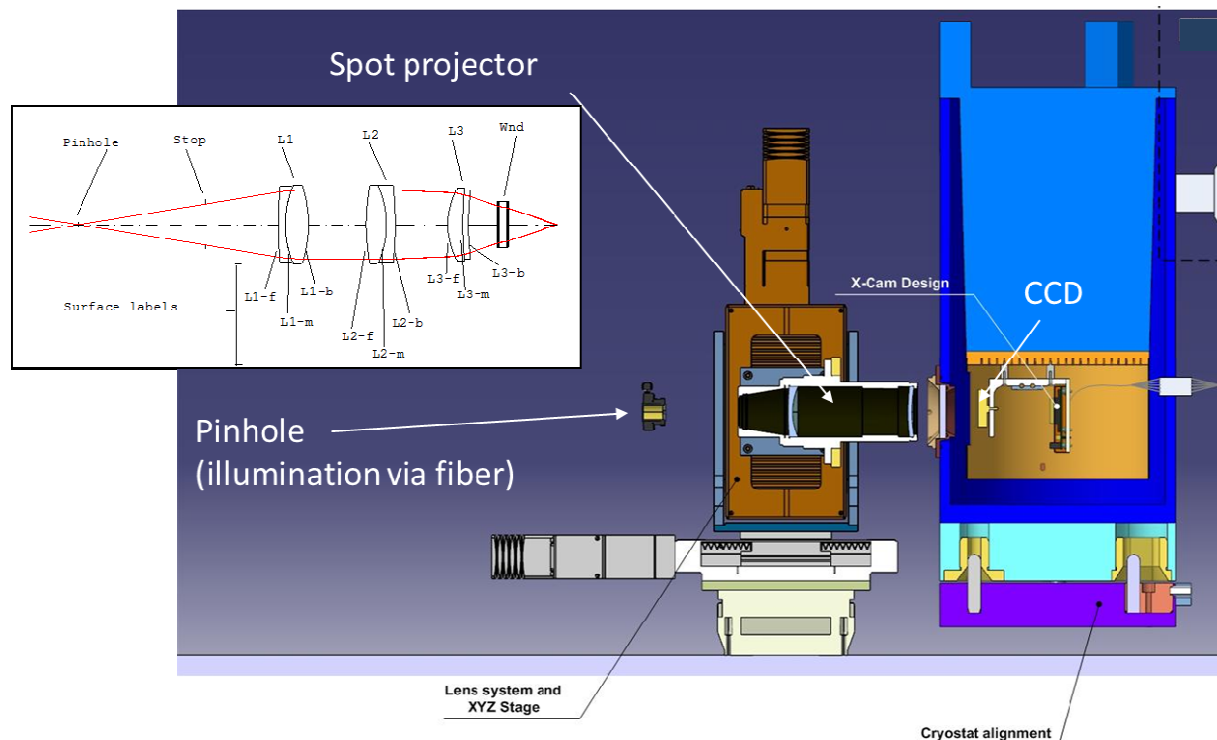


Figure 10: schematic of the set-up for the scanning sub-pixel spot projector. The design of the optics is shown in the insert on the left. The element labeled 'Wnd' is not part of the optics assembly but represents the sapphire cryostat vacuum window.

The design of the optics was constrained by the requirement to get the sufficiently small spots over the entire Euclid wavelength band in the presence of an 8 mm thick sapphire vacuum window. The sapphire window was part of the deliverable optics and all performance tests were done with the combination of optics and window. The design values for 84% Encircled Energy (EE) diameters, as well as values predicted from wavefront measurements and values measured with relatively broad band light are listed in Table 2. It is clear that the band width of the light will have to be limited to a few nm.

Table 2: design values and measured and predicted 84% EE diameters.

Wavelength (nm)	84% encircled energy diameter (μm)				
	Design value mono-chromatic	Calculated* from wavefront measurements, monochromatic	Calculated* from wavefront measurements, $\Delta\lambda = 3\text{nm}$	Measured* with $\Delta\lambda = 8.6, 12.6, 14.7\text{ nm, resp.}$	Calculated* for $\Delta\lambda = 8.6, 12.6, 14.7\text{ nm}$
550	4.1	4.1	8.2	35	33
750	3.5	6.0	7.2	28	25
920	4.9	4.8	5.2	32	19

*Measurements and calculations by Jenoptik Optical Systems

The spot projector will be used for three different experiments.:

- *Sub-pixel scan*: this involves the recording of a 2-D map (in steps of $2\mu\text{m}$) of several pixels to determine the sub-pixel and inter-pixel response non uniformity and also the sub-pixel response variation from pixel to pixel. For each position one or several images are taken and then the corresponding sub-pixel map is created. By further deconvolution of the well-calibrated optical spot PSF, the detector sub-pixel response, and from this, the charge carrier diffusion length can be determined. This can be repeated for different temperatures, wavelengths and substrate voltages, and in variations of pixel phases ON or OFF.

- *Multiple object illumination:* during a typical Euclid integration time of ~600 seconds it is possible to illuminate several locations (in sub-pixel mode or in 'Euclid mode', achieved with reduced aperture stop size) on the CCD by moving the spot projector. The operation could be done on several areas on the CCD. Similar to the multi-spot experiment described in section 2.6 this enables the direct comparison of irradiated and non-irradiated areas, with the advantages that the PSF shape can be exactly the same on each location, of arbitrary shape, and in any pattern.

- *Euclid-like field illumination:* The goal of this test is to image realistic star/galaxy fields by illuminating a full CCD with star-like and extended-objects to simulate the complete calibration process (interpolation of the PSF using the star and determination of the ellipticity of the galaxies). The spot projector is not able to image large fields directly, but the multiple object illumination approach with the spot in sub-pixel mode can be used for simplified scenes:

- Bright stars (mag 18) are produced by direct focused illumination

- Faint objects (mag 24.5) are produced by defocused or smeared (using the translation stages) illumination. The 6.5 magnitude difference with bright stars, could be achieved by varying the illumination duration. Within 600 seconds, only a limited number of objects could be generated (ideally at least 50 stars and one or two faint objects), but this should allow PSF calibration study and comparison between irradiated and non-irradiated areas, with identical PSF and identical faint objects with representative magnitude differences.

Finally, the setup could be used to generate faint objects with color gradient or stars with color content, indeed by multiple passes over the same object with different wavelengths and different illumination passes, colored structure/content could be "imprinted".

The spot projector's PSF calibration has started and the first CCD experiments are foreseen with a few months.

3. SUMMARY

We have described ESA's CCD test bench that is foreseen to support detector development and characterization, and to enable an independent assessment of the Euclid VIS CCDs. The bench's ability to measure basic CCD performance parameters such as read noise, CTE, QE, PRNU, full well capacity etc. from x-ray and uniform optical illumination has been demonstrated. Of particular importance for Euclid is the ability to characterize spot shapes and their variation due to the effects of radiation damage on charge transfer efficiency. Preliminary results have been shown from an experiment with a multi-pinhole mask which projects the equivalent of small extended objects on the CCD. A more advanced scanning spot projector for intra-pixel response characterization has been built and will shortly be commissioned.

ACKNOWLEDGMENTS

We wish to acknowledge the support of Neil Murray (Open University, Milton Keynes, UK) in getting familiar with the XCAM CCD controller and its operation. Also acknowledged is the continuous support of Ralf Kohley (ESA/ESAC).

REFERENCES

- [1] Laureijs, R. et al., "Euclid: ESA's mission to map the geometry of the universe", to be published in SPIE proceedings 8442, (2012)
- [2] Cropper, M. et al. "VIS: the visible imager for Euclid", to be published in SPIE proceedings 8442, (2012).
- [3] Prieto, E. et al. "Euclid NISP instrument concept at the end of the phase A study", to be published in SPIE proceedings 8442, (2012)
- [4] Crouzet, P.-E. et al., "Test set-up description and performance for HAWAII 2RG detector characterization at Estec", to be published in SPIE proceedings 8453, (2012).
- [5] Boudin, N. et al., "Preliminary results of CCD characterisation at ESA in support of the Euclid visible channel", to be published in SPIE proceedings 8453, (2012).
- [6] Paulin-Henriksson, S. et al., "Point spread function calibration requirements for dark energy from cosmic shear", A&A 484, 67-77, (2008).